

# Silica Nanoparticles Loaded With Selenium Quantum Dots Reduce Myocardial Ischemia-Reperfusion Injury by Alleviating Ferroptosis and Mitochondrial Dysfunction

Taixi Li<sup>1</sup>\*, Boshen Yang<sup>1</sup>\*, Xijian Liu<sup>2</sup>, Dongmei Shi<sup>1</sup>, Zhixiang Wang<sup>1</sup>, Yizhi Chen<sup>1</sup>, Chengxing Shen<sup>1</sup>

<sup>1</sup>Department of Cardiology, Shanghai Sixth People's Hospital Affiliated to Shanghai Jiao Tong University School of Medicine, Shanghai, 200233, People's Republic of China; <sup>2</sup>School of Chemistry and Chemical Engineering, Shanghai Frontiers Science Research Center for Druggability of Cardiovascular Noncoding RNA, Shanghai Engineering Technology Research Center for Pharmaceutical Intelligent Equipment, Shanghai University of Engineering Science, Shanghai, 201620, People's Republic of China

\*These authors contributed equally to this work

Correspondence: Chengxing Shen, Department of Cardiology, Shanghai Sixth People's Hospital Affiliated to Shanghai Jiao Tong University School of Medicine, Shanghai, 200233, People's Republic of China, Email shencx@sjtu.edu.cn

**Purpose:** Myocardial ischemia-reperfusion (IR) injury, a significant challenge in cardiovascular treatment, is primarily driven by ferroptosis and mitochondrial dysfunction. Despite extensive research, no clinical therapies effectively target ferroptosis in IR injury. This study aims to develop selenium-quantum-dot-loaded porous silica nanospheres (Se@PSN) as a novel therapeutic approach to address IR injury.

**Patients and Methods:** Se@PSN were synthesized and tested for their reactive oxygen species (ROS) scavenging capabilities and biocompatibility. Additionally, the effects of Se@PSN on ferroptosis, mitochondrial damage, oxidative stress, and myocardial IR injury severity were evaluated.

**Results:** Se@PSN enhanced the stability of selenium quantum dots and exhibited strong ROS scavenging abilities. Additionally, Se@PSN exhibited excellent biocompatibility. The Se@PSN treatment increased GPX4 levels, effectively inhibiting ferroptosis in cardiomyocytes. Furthermore, Se@PSN promoted the expression of mitochondrial respiratory complexes, mitigating oxidative phosphorylation damage and preserving mitochondrial function. These effects collectively resulted in reduced myocardial loss, inflammation, and fibrosis following IR injury. Compared to PSN alone, Se@PSN showed superior therapeutic efficacy against IR injury.

**Conclusion:** Se@PSN exhibit great potential in reducing ferroptosis and protecting mitochondrial function, making them a promising therapeutic approach for the treatment of myocardial IR injury.

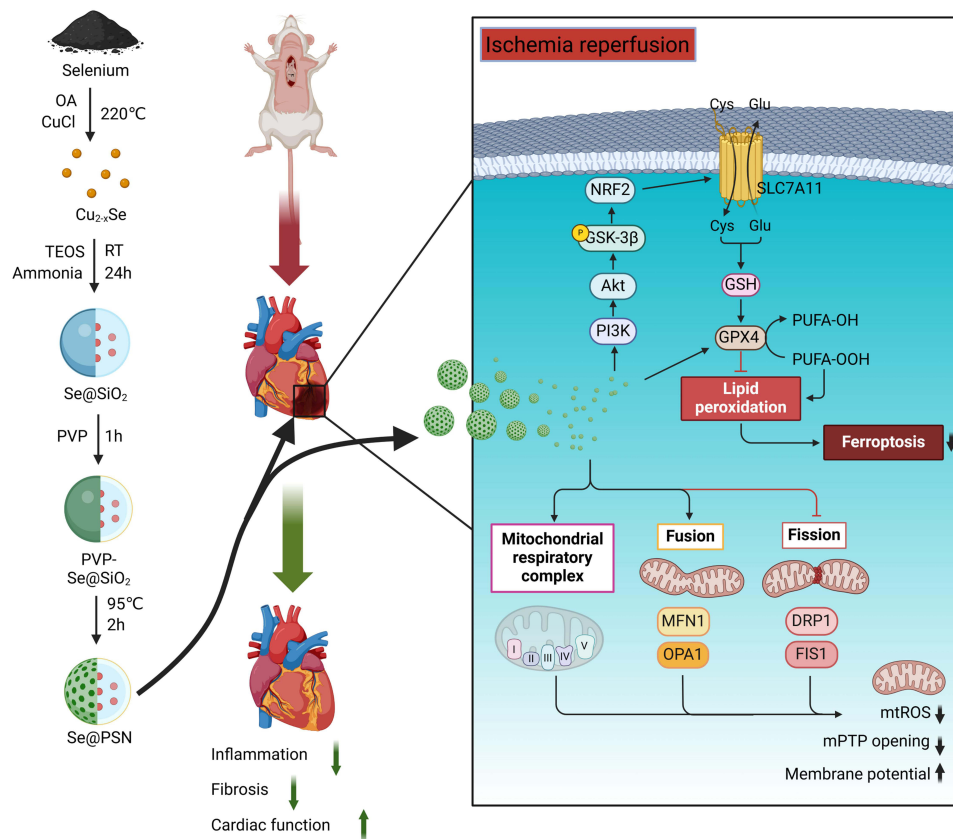
**Keywords:** myocardial ischemia reperfusion, selenium, porous silica nanospheres, ferroptosis, reactive oxygen species

## Introduction

Myocardial ischemic injury, a challenging problem for clinicians, is a leading cause of disability and death, accounting for 1.72% of the global population.<sup>1-3</sup> During ischemia, myocardial cells cannot receive adequate oxygen and nutrients. Prolonged ischemia can lead to progressively irreversible structural and functional changes in the myocardium.<sup>4</sup> Percutaneous coronary intervention (PCI) and medications are commonly used to restore myocardial blood flow.<sup>5</sup> However, the sudden restoration of blood flow to the myocardium can cause further damage beyond the initial ischemic injury, a phenomenon known as myocardial ischemia/reperfusion (IR) injury. This injury results in no-reflow phenomenon, arrhythmias, and myocardial cell death post-treatment.<sup>6</sup> The low proliferative capacity of cardiomyocytes makes



## Graphical Abstract



the extent of myocardial cell loss a crucial factor in determining cardiac function.<sup>7</sup> However, there are currently few therapies or drugs that effectively protect myocardial cells from IR injury.

In the past decade, several types of cell death pathways have been shown to play critical roles in the progression of myocardial IR, such as apoptosis and pyroptosis.<sup>8,9</sup> Recently, ferroptosis has also been found to play a destructive role in myocardial infarction and myocardial IR injury. Ferroptosis is a form of iron-dependent regulated cell death. During IR, the degradation of ferritin releases iron ions, triggering the Fenton reaction to generate reactive oxygen species (ROS), leading to lipid peroxidation and subsequent cardiac damage.<sup>10–12</sup> Ferroptosis is closely linked to mitochondrial damage. Excess ROS generated during ferroptosis can disrupt mitochondria by inducing the opening of the mitochondrial permeability transition pore (mPTP), intracellular Ca<sup>2+</sup> overload, and oxidative damage to mitochondrial DNA (mtDNA).<sup>13</sup> This cascade of events disrupts the mitochondrial electron transport chain (ETC), impairs oxidative phosphorylation (OXPHOS), and compromise mitochondrial respiration. Importantly, OXPHOS dysfunction results in the excessive production of mitochondrial ROS, which further exacerbating ferroptosis and creating a vicious cycle.<sup>14</sup> Therefore, an effective strategy is needed to rescue functional mitochondria and reduce ferroptosis during IR injury.

Glutathione peroxidase 4 (GPX4), the primary endogenous defense against lipid peroxidation, reduces lipid peroxides to lipid alcohols using glutathione (GSH).<sup>15–17</sup> Additionally, GPX4 is also present in mitochondria, where it helps prevent excessive mitochondrial ROS production and maintains normal mitochondrial respiration. Activating GPX4 may be a potential strategy for treating myocardial IR. Notably, GPX4 is a selenoprotein, and adequate selenium intake can enhance the expression and activity of GPX4 in cells.<sup>18</sup> Selenium deficiency significantly reduces glutathione peroxidase activity and increases oxidative stress.<sup>19</sup> Despite its widespread use in dietary supplements, selenium has a narrow therapeutic window, limiting its clinical application in IR injury.<sup>20</sup>

However, advancements in nanotechnology offer potential solutions to the challenges associated with selenium-containing drugs. Selenium quantum dots (SeQDs) represent a promising new strategy to inhibit ferroptosis, characterized by their minimal cytotoxicity and high biocompatibility. They exhibit strong reducing properties, enabling them to neutralize ROS produced during IR. Additionally, once inside cells, SeQDs serve as a precursor for selenocysteine synthesis, which is crucial for the formation of GPX4 and the treatment of ferroptosis.<sup>21</sup> However, SeQDs generally have diameters smaller than 5 nm, which limits their retention within cells. Furthermore, their negatively charged surfaces hinder effective cellular absorption. Consequently, it is essential to design suitable carriers that can enlarge SeQD size and alter their surface characteristics. Porous silica nanoparticles (PSNs), with their large pore volume, surface functional groups, and excellent biocompatibility, have been considered excellent carriers in the therapeutic and pharmaceutical fields. Compared to other inorganic nanoparticles, another advantage of PSNs is their relatively superior biocompatibility and biodegradability. PSNs have been demonstrated to serve as excellent carriers for various drugs in the treatment of myocardial ischemia, with surface modifications enhancing their therapeutic efficacy.<sup>22–24</sup> Encapsulating SeQDs within PSNs may enhance their pharmacokinetics and improve their bioavailability.

In this study, we synthesized a nanoparticle, Se@PSN, as a novel strategy to inhibit ferroptosis. SeQDs were encapsulated within PSNs, and the surface was coated with polyvinyl pyrrolidone (PVP) to enhance biocompatibility. Se@PSN retained the reductive properties of SeQDs, allowing it to effectively scavenge various ROS. More importantly, applying Se@PSN to the reperfusion area partially alleviated mitochondrial structural and functional damage, as well as ferroptosis, thereby helping to preserve cardiac function. In light of these findings, our work offers a novel and promising approach for using SeQDs to treat myocardial IR injury and other ferroptosis-related diseases.

## Material and Methods

### Preparation of Se@PSN and FITC-Se@PSN

Se@PSN was synthesized following a previously established protocol.<sup>25</sup> Briefly, 39.5 mg of selenium powder was added to 5 mL of oleic acid (OA) preheated to 120°C under a nitrogen atmosphere, with stirring for 30 minutes. The temperature was then raised to 280°C and held for 30 minutes. After cooling to 220°C, the Se-OA precursor was obtained for further use. In a separate flask, 5 mL of oleylamine (OAM), 5 mL of OA, and 49.5 mg of CuCl were heated to 120°C under nitrogen and stirred for 30 minutes. The temperature was then increased to 220°C for an additional 5 minutes. The Se-OA precursor was quickly injected into the CuCl mixture and aged at 220°C for 5 more minutes, followed by rapid cooling to 60°C. Ethanol was added to the mixture, and it was centrifuged three times with ethanol. The resulting  $\text{Cu}_{2-x}\text{Se}$  nanocrystals were then dispersed in 10 mL of hexane for future use.

To synthesize Se@SiO<sub>2</sub> core-shell nanospheres, 5 mL of the  $\text{Cu}_{2-x}\text{Se}$  hexane solution was mixed with 30 mL of n-hexane, 3 mL of n-hexanol, 3 mL of Triton X-100, 0.9 mL of deionized water, and 0.05 mL of tetraethyl orthosilicate. The mixture was stirred rapidly, and 0.1 mL of ammonium hydroxide was added to facilitate the formation of  $[\text{Cu}(\text{NH}_3)_4]^{2+}$ . The mixture was stirred at room temperature for 24 hours, after which solid Se@SiO<sub>2</sub> particles were isolated by adding ethanol. The solid Se@SiO<sub>2</sub> nanospheres were collected by centrifugation and washed three times with ethanol.

The freshly prepared solid Se@SiO<sub>2</sub> nanospheres were dispersed in 20 mL of a 10 g L<sup>-1</sup> PVP solution (K30) and stirred for 1 hour. The mixture was then heated to 95°C and maintained at this temperature for 2 hours. The Se@PSN were collected by centrifugation and washed three times with ethanol.

To track the nanoparticles, FITC-Se@PSN was synthesized. Se@PSN was first ultrasonically dispersed in ethanol, after which 0.3 g of 3-aminopropyltriethoxysilane (APTES) and 150 μL of water were added. The solution was stirred at 50°C for 24 hours to produce amino-modified Se@PSN, which was then dried at room temperature. Fluorescein isothiocyanate (FITC), dissolved in dimethyl sulfoxide (DMSO), was added to 100 mL of ethanol, and the amino-modified Se@PSN was ultrasonically dispersed into this solution. The mixture was stirred in the dark at 50°C for 5 hours. After centrifugation and washing with ethanol three times, FITC-Se@PSN was obtained.

## Characterization of Se@PSN

Transmission electron microscopy (TEM) imaging was conducted at 200 keV using the TALOS F200X microscope (ThermoFisher, USA). X-ray diffraction (XRD) patterns were recorded with a D8 ADVANCE Da Vinci instrument (Bruker, USA). The morphology and elemental mapping of Se@PSN were characterized using a scanning electron microscope (SEM, Sigma 300, Carl Zeiss AG, Germany) equipped with an energy dispersive spectrometer (EDS) system, operated at 20 keV with a magnification of 4819X and a working distance of 8.5 mm. The particle size and zeta potential of solid Se@SiO<sub>2</sub> and Se@PSN in phosphate buffer solution (PBS) were measured at 25°C using an Omni instrument (Brookhaven, USA). Atomic force microscope (AFM) imaging was performed with a FastScan Bio (Bruker, USA). Nitrogen adsorption measurements were conducted using the Autosorb-IQ3 instrument (Quantachrome, USA).

## Antioxidant Activity Measurements

### ABTS Scavenging Activity Assay

Total free radical scavenging activity was assessed using an ABTS assay kit (S0119, Beyotime, China). Absorbance was measured at 734 nm using a microplate reader (Epoch, BioTek, USA).

### •OH Scavenging Activity Assay

The •OH scavenging activity of Se@PSN was evaluated using the methyl violet (MV)-Fenton reagent system. Different concentrations of Se@PSN or Se@SiO<sub>2</sub> were diluted in 0.1 M Tris-HCl buffer (pH 4.7) and reacted with 0.5 mm FeSO<sub>4</sub> and 50 mm H<sub>2</sub>O<sub>2</sub> to generate •OH. After incubating with 0.15 mm MV for 10 minutes at room temperature, absorbance at 582 nm was recorded using a microplate reader (Epoch, BioTek, USA).

### •O<sub>2</sub><sup>-</sup> Scavenging Activity Assay

The •O<sub>2</sub><sup>-</sup> radical scavenging activity of Se@PSN was assessed using the nitrated blue tetrazolium (NBT)-riboflavin method. 100 µL of riboflavin (1.2 mm) was added to a solution containing NBT (2 mm), EDTA (400 µL, 0.1 M), and PBS (5.8 mL, pH 7.8, 10.0 mm). Different concentrations of Se@PSN or Se@SiO<sub>2</sub> (50 µL) were mixed with 100 µL of this detection solution. The mixtures were shaken at 37°C for 5 minutes and exposed to light for 2 minutes. Absorbance was measured at 560 nm.

### H<sub>2</sub>O<sub>2</sub> Scavenging Activity Assay

The H<sub>2</sub>O<sub>2</sub> scavenging ability of Se@PSN was measured using the xylenol orange (XO)-FeSO<sub>4</sub> method. The detection solution was prepared by mixing 0.45 mm FeSO<sub>4</sub>, 0.45 mm XO, and various concentrations of Se@PSN or Se@SiO<sub>2</sub> in Tris-HCl buffer (180 µL, pH 4.7, 0.1 M). H<sub>2</sub>O<sub>2</sub> was then added to achieve a final concentration of 100 µM. The mixtures were incubated in the dark at 37°C for 30 minutes, and absorbance was measured at 550 nm.

## Measurement of Selenium Concentrations Using Inductively Coupled Plasma Mass Spectrometry (ICP-MS)

To assess the release of selenium from Se@PSN, 40 mg of Se@PSN was dispersed in 5 mL of PBS using ultrasound and incubated in a shaker at 37°C for 1, 2, 3, 4, and 5 days. The supernatant was collected by centrifugation, filtered through a 0.22 µm filter, and treated with 2 mL of aqua regia. Selenium content was then quantified using ICP-MS (NexION5000G, PERKINELMER, USA).

For organ accumulation studies, mice (20–25 g, 8–10 weeks old) were injected with Se@PSN into the myocardium immediately after the release of left anterior descending (LAD) ligation. Each mouse received an intramyocardial injection of 40 ng of Se@PSN dispersed in 10 µL of saline, administered slowly into the left ventricular wall using a 25G needle. Hearts were harvested at 6, 12, 24, and 48 hours post-injection, weighed, dissolved in aqua regia, and analyzed for selenium content using ICP-MS.

## Murine IR Model

Myocardial IR injury was induced by ligating the LAD coronary artery for 45 minutes followed by removal of the ligature. Mice were anesthetized with 1.5% isoflurane and ventilated using a 16-gauge catheter. An adjustable knot of 8-0 monofilament nylon suture was placed around the LAD approximately 1.5 to 2 mm below the left atrial appendage. Successful ligation was indicated by blanching of the anterior wall of the left ventricle. The chest was then closed, with the suture ends left outside the thoracic cavity, and air was removed from the chest cavity. After 45 minutes, the mice were re-anesthetized, and the ligature was carefully released to restore blood flow. Sham-operated mice underwent the same procedure without LAD ligation. 24 hours after reperfusion, the mice were re-anesthetized, and the heart was excised for most of the analyses, except for myocardial fibrosis, which was sampled and assessed on day 14 after reperfusion.

## Ex Vivo Fluorescence Imaging

To track the accumulation of Se@PSN in major organs, FITC-Se@PSN was injected directly into the anterior wall of the left ventricle of mice immediately following the release of LAD ligation. Hearts were harvested at 12, 24, and 48 hours post-injection. The tissues were kept on ice chilled plastic dishes until dissection, then transferred onto fluorescence-blocking paper and imaged in a pre-warmed IVIS Spectrum chamber (PERKINELMER, USA).

## Safety Evaluations of Se@PSN in Mice

The potential side effects of Se@PSN treatment were evaluated in healthy mice administered Se@PSN. Mice were injected with a therapeutic dose (40 ng) of Se@PSN into the myocardium and sacrificed on days 1, 7, and 14. Serum levels of alanine aminotransferase (ALT), aspartate aminotransferase (AST), blood urea nitrogen (BUN), and creatinine (CREA) were analyzed. Major organs, including the hearts, lungs, liver, kidneys, and spleen, were examined using hematoxylin-eosin (H&E) staining.

In addition, the myocardial toxicity of Se@PSN at 8 times the therapeutic dose was also assessed to detect the side effects of high doses. Cardiac function, serum levels of creatine kinase-MB (CK-MB) and cardiac troponin I (cTnI) were measured 24 hours after reperfusion, and serum lactate dehydrogenase (LDH) levels were analyzed 48 hours after reperfusion. Cardiac function was re-assessed 14 days after reperfusion.

## Cell Culture

The H9c2 cells used in this study were obtained from ATCC. H9c2 cells were maintained in high-glucose Dulbecco's Modified Eagle Medium (DMEM, ThermoFisher, USA) supplemented with 10% FBS and 1% penicillin-streptomycin. Incubation was carried out at 37°C in a HERACELL 150i (ThermoFisher, USA) under a humidified atmosphere containing 5% carbon dioxide.

To establish hypoxia-reoxygenation (HR) injury models, H9c2 cells were first incubated in glucose-free medium under hypoxic conditions (95% nitrogen, 5% carbon dioxide) for 6 hours at 37°C. Afterward, the medium was replaced with DMEM, and cells were cultured under normoxic conditions for an additional 12 hours. For the HR+ Se@PSN and HR+ PSN groups, Se@PSN or PSN (80 µg/mL) were added at the time of medium replacement after 6 hours of hypoxia, and the cells were co-cultured for another 12 hours. In the Se@PSN group, H9c2 cells were cultured under normoxic conditions with Se@PSN (80 µg mL<sup>-1</sup>) for 12 hours.

To induce ferroptosis, H9c2 cells were cultured in DMEM containing erastin (1 µM) for 24 hours. For the Erastin + Se@PSN and Erastin + PSN groups, Se@PSN or PSN (80 µg mL<sup>-1</sup>) were added simultaneously with erastin to the medium, and the cells were co-cultured for 24 hours. In the Se@PSN group, H9c2 cells were cultured in DMEM with Se@PSN (80 µg mL<sup>-1</sup>) for 24 hours.

## Cell Biocompatibility Assay

The biocompatibility of Se@PSN was assessed by evaluating its inhibitory effect on H9c2 cell proliferation. H9c2 cells were seeded at an appropriate density in 96-well plates and exposed to varying concentrations of Se@PSN

(0–160  $\mu\text{g mL}^{-1}$ ) for 24 hours. Cell proliferation was measured using the Cell Counting Kit-8 (Dojindo, Japan), and absorbance was recorded at 450 nm using a microplate reader (Epoch, BioTek, USA). To select the optimal treatment concentration, different concentrations of Se@PSN were added at the time of medium replacement after 6 hours of hypoxia, and the cells were co-cultured for an additional 12 hours. Cell proliferation was measured in the same manner, and the concentration with the highest cell proliferation was selected as the treatment concentration.

## In Vitro Uptake Experiments

H9c2 cells were seeded at an appropriate density in confocal culture dishes and cultured overnight to allow attachment. FITC-Se@PSN (80  $\mu\text{g mL}^{-1}$ ) was added to each well at different time. After PBS washes, cells were incubated with DAPI for 10 minutes. Fluorescence imaging was performed using an A1 laser confocal microscope (Nikon, Japan), and fluorescence intensity was analyzed using ImageJ software.

## RNA Sequencing Analysis

Total RNA was extracted from mouse hearts one day after IR. RNA quality was assessed using the 2100 Bioanalyzer (Agilent), and RNA quantification was performed with the NanoDrop 2000 spectrophotometer (ThermoFisher, USA). Following cDNA synthesis and library quality evaluation, RNA sequencing was carried out on the Illumina HiSeq X10 platform (Illumina, USA) provided by Novogene (China). Transcript expression levels were calculated using the fragments per kilobase of exon model per million mapped fragments (FPKM) method, and bioinformatics analysis was conducted using online databases and platforms.

## Western Blotting

Heart tissues from mice in different groups were immediately stored at  $-80^{\circ}\text{C}$  after euthanasia. H9c2 cells were washed three times with PBS. Both tissue and cell samples were lysed using lysis buffer (P0013B, Beyotime, China) supplemented with protease inhibitors (P1005, Beyotime, China) and phosphatase inhibitors (P1045, Beyotime, China). Protein concentration was determined using a BCA Protein Assay Kit (23225, ThermoFisher, USA). Proteins were separated by sodium dodecyl sulfate-polyacrylamide gel electrophoresis (SDS-PAGE) and transferred onto polyvinylidene fluoride (PVDF) membranes. After a 2-hour transfer, the membranes were blocked and washed three times for 5 minutes each. They were then incubated with primary antibodies overnight at  $4^{\circ}\text{C}$ . Following three washes with Tris-buffered saline containing Tween 20 (TBST), the membranes were incubated with horseradish peroxidase (HRP)-conjugated secondary antibodies at room temperature for 1 hour. Protein bands were visualized using enhanced chemiluminescence (ECL) and analyzed using ImageJ software.

## Immunohistochemistry

The tissue sections were deparaffinized and rehydrated. Endogenous peroxidase activity was blocked using 3%  $\text{H}_2\text{O}_2$ . Antigen retrieval was performed by heating the sections in citrate buffer at  $95^{\circ}\text{C}$  for 20 minutes, followed by cooling to room temperature. The samples were incubated with the primary antibody overnight at  $4^{\circ}\text{C}$ , and then stained with the secondary antibody for 30 minutes at room temperature. DAB substrate solution was added to visualize antibody staining, and the slides were mounted. Images were captured using an Olympus IX71 microscope, and staining intensity was quantified using ImageJ software.

## Isolation and Quantification of RNA via qRT-PCR

Total RNA was extracted from heart tissue or H9c2 cells using Trizol reagent. The purity of the RNA was assessed by UV spectrophotometry (NanoDrop 2000, ThermoFisher, USA) and electrophoresis. cDNA was synthesized using the HiScript II Q RT SuperMix kit (Vazyme, China). Real-time PCR was performed using the AceQ Universal SYBR qPCR Master Mix (Vazyme, China). The primer sequences are provided in [Table 1 of the supplementary materials](#).

## Immunofluorescence Staining

For tissue staining, mice were euthanized, and the tissues were quickly isolated, fixed in 4% paraformaldehyde, and embedded in paraffin. The embedded tissue sections were cut to a thickness of 5  $\mu\text{m}$ . Sections were then deparaffinized using xylene and ethanol, followed by antigen retrieval in 10 mM sodium citrate buffer (pH 6.0) for 10 minutes. For cell staining, H9c2 cells were seeded on glass coverslips and fixed with 4% paraformaldehyde at 37°C for 15 minutes, then stored in PBS at 4°C. Both the fixed tissue sections and cell coverslips were permeabilized with 0.1% Triton X-100 for 30 minutes at room temperature and blocked with 3% goat serum for 1 hour. The slides were incubated overnight at 4°C with primary antibodies. After PBS washing, the samples were stained with fluorescent secondary antibodies, followed by DAPI (C1002, Beyotime, China) staining. Images were captured using an IX71 fluorescence microscope (OLYMPUS, Japan), and fluorescence intensity was analyzed with ImageJ software.

## GPx and SOD Activity Assays

After homogenizing the heart tissue, the samples were centrifuged at 12,000g for 10 minutes at 4°C, and the supernatant was collected for further analysis. SOD activity was measured using a Total Superoxide Dismutase Assay Kit (S0109, Beyotime, China), and GPx activity was assessed with a Total Glutathione Peroxidase Assay Kit (S0058, Beyotime, China).

## FerroOrange Staining In Vitro

After different treatments, the medium was removed from the H9c2 cells, and the cells were washed three times with HBSS. FerroOrange working solution (F374, Dojindo, Japan) was added, and the cells were incubated for 30 minutes at 37°C in 5% CO<sub>2</sub>. The stained cells were counterstained with DAPI and washed with PBS. Fluorescence images were captured using an IX71 microscope, and intensity was analyzed using ImageJ software.

## BODIPY-C11 Staining In Vitro

After different treatments, the medium was removed from the H9c2 cells, and the cells were washed twice with fresh medium. After discarding the supernatant, the BODIPY-C11 working solution (F374, Dojindo, Japan) was added, and the cells were incubated for 30 minutes at 37°C in a 5% carbon dioxide incubator. Following incubation, the working solution was removed, and the cells were washed twice with HBSS. The stained cells were counterstained with DAPI and washed with PBS. Fluorescence images were captured using an IX71 microscope, and intensity was analyzed using ImageJ software.

## TEM Observation of Mitochondria

Heart tissues were fixed overnight in 4% glutaraldehyde at 4°C, followed by a 1-hour fixation in 1% osmium tetroxide. The tissues were then dehydrated, embedded in epoxy resin, and sectioned into 60 nm slices. The sections were stained with 2% uranyl acetate and lead citrate, and observed using a TEM (Hitachi, Japan).

## MitoSOX, JC-1, and mPTP Determination In Vitro

Mitochondrial ROS in H9c2 cells were detected using the MitoSOX Red Mitochondrial Superoxide Indicator (ABclonal, China). The indicator was diluted to 5  $\mu\text{M}$  in Hanks' Balanced Salt Solution (HBSS) and added to the cell samples, which were incubated in the dark at 37°C for 10 minutes. After incubation, the cells were washed and resuspended in HBSS.

Mitochondrial membrane potential was assessed using the JC-1 Assay Kit (C2006, Beyotime, China). Cells were incubated with JC-1 staining solution at 37°C for 20 minutes, followed by two washes with staining buffer.

The mPTP opening was evaluated using the mPTP Assay Kit (C2009S, Beyotime, China). H9c2 cells were incubated with calcein-AM at 37°C for 30 minutes, followed by an additional 20-minute incubation with CoCl<sub>2</sub> at 37°C. After incubation, the cells were washed and resuspended in HBSS.

The stained cells were counterstained with DAPI and washed with PBS. Fluorescence images were captured using an IX71 microscope, and intensity was analyzed using ImageJ software.

## Measurement of Cellular ROS Levels

Cellular ROS production was measured using the DCFH-DA detection kit (S0033M, Beyotime, China). H9c2 cells were incubated with the DCFH-DA probe in the dark for 30 minutes, followed by fluorescence imaging with a fluorescence microscope.

## Evaluation of Cardiac Function

Echocardiography was used to assess the impact of IR on cardiac function. Mice were anesthetized with 1.5% isoflurane and placed on a temperature-controlled platform (37°C). Cardiac function was analyzed using a high-resolution ultrasound system for small animals (Vevo3100, Fujifilm Visual Sonics, Japan). M-mode images of the left ventricle were captured to evaluate FS, EF, [LV Vol;d], and [LV Vol;s].

## Triphenyltetrazolium Chloride (TTC) and Evans Blue Staining

After anesthetizing the mice, the chest cavity was opened, and the LAD artery was re-ligated. A 0.1 mL solution of 1% Evans Blue was injected into the left ventricle via the apex. Hearts were harvested from the euthanized animals and flushed with cold PBS (4°C) to remove residual blood. The heart tissues were then frozen at -20°C for 20 minutes and sliced into 2 mm sections along the short axis. The slices were incubated in 1% TTC solution at 37°C for 30 minutes in the dark, fixed in tissue fixative for 3 hours, and rinsed with PBS. Images were captured and analyzed using ImageJ software.

## Measurement of Serum Cardiac Injury Markers

Blood was collected from the carotid artery of anesthetized mice and centrifuged at 3000 rpm for 10 minutes to obtain serum, which was immediately stored at -80°C for testing within one week. LDH and CK-MB levels were measured using an automated biochemical analyzer (Chemray 240, Rayto, China), while cTnI was detected using a Mouse cTnI ELISA Kit (E08421m, CUSABIO, China) following the manufacturer's instructions. CK-MB and cTnI were measured 24 hours after reperfusion, while LDH levels were assessed 48 hours after reperfusion.

## TUNEL Staining

TUNEL staining was performed using a commercial kit (C1089, Beyotime, China) according to the manufacturer's instructions. Deparaffinized heart sections were incubated with DNase-free proteinase K (20 µg mL<sup>-1</sup>) at room temperature for 30 minutes, followed by incubation with the TdT reaction mixture at 37°C for 60 minutes in the dark. After washing with PBS, the sections were counterstained with DAPI and observed under an Olympus IX71 fluorescence microscope.

## Animal Study

Eight-week-old male C57BL/6J mice were obtained from Charles River, China. The mice were housed in a specific pathogen-free facility under controlled conditions: a temperature of 24°C, a 12-hour light/dark cycle, and 40–60% humidity, with free access to food and water. All animal experiments were conducted in accordance with the animal care guidelines of Shanghai Jiao Tong University (IACUC approval number: A2023116).

## Statistical Analysis

Data were analyzed using GraphPad Prism version 8 (GraphPad Software; [www.graphpad.com](http://www.graphpad.com)). Statistical significance between groups was assessed using one-way ANOVA and t-tests, with differences considered significant at  $p < 0.05$ .

## Results

### Characterization of Se@PSN

Se@PSN were synthesized using methods previously described.<sup>25</sup> Initially, SeQDs were created by oxidizing Cu<sub>2-x</sub>Se nanocrystals, which were then coated with silica using a one-pot method to produce solid Se@SiO<sub>2</sub> nanospheres. TEM images revealed the morphology of the nanoparticles (Figure 1A), with numerous small quantum dots distributed from the center to the surface (Figure 1B). Then the solid Se@SiO<sub>2</sub> nanospheres were coated with PVP and etched in hot water to form Se@PSN

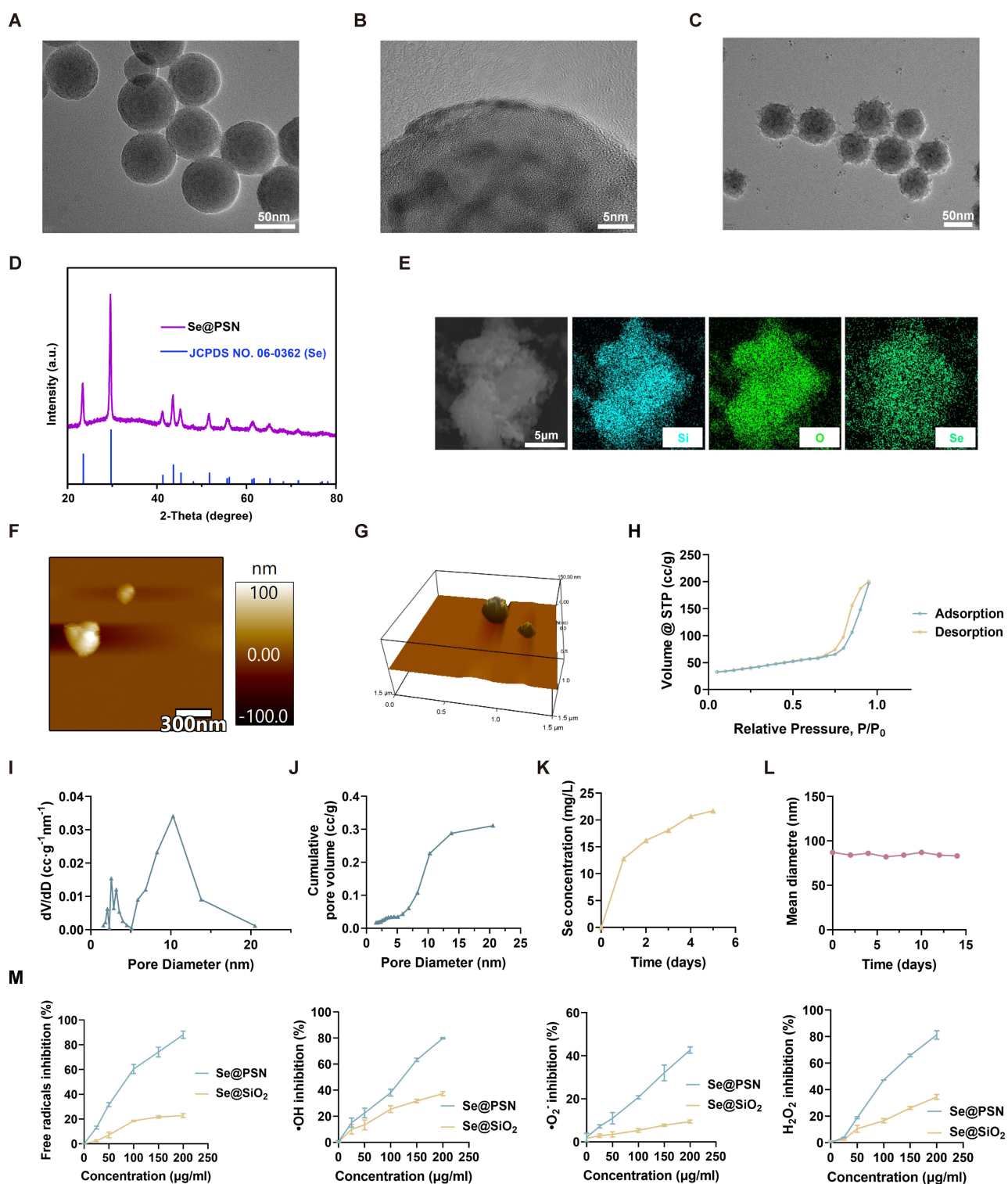


**Figure 1** Characterization of Se@PSN. (**A** and **B**) Low and high magnification TEM images of solid Se@SiO<sub>2</sub>. (**C**) TEM image of Se@PSN. (**D**) XRD patterns of Se@PSN and standard selenium phase. (**E**) Elemental mapping showing the distribution of Si, O, and Se. (**F** and **G**) AFM analysis of Se@PSN, with height and 3D surface images. (**H**) Nitrogen adsorption-desorption isotherms of Se@PSN. (**I**, **J**) Pore size distribution and cumulative pore volume of Se@PSN. (**K**) Release profile of selenium concentration from 8g L<sup>-1</sup> Se@PSN. (**L**) Average hydration diameter of Se@PSN in PBS within 14 days. (**M**) Free radical and ROS inhibition assays demonstrating the dose-dependent neutralization of total free radicals, •OH, •O<sub>2</sub><sup>-</sup>, and H<sub>2</sub>O<sub>2</sub> by Se@PSN and Se@SiO<sub>2</sub> (n=3).

(Figure 1C, Figure S1). The PVP modification was evident from the change in zeta potential measurements, where the solid Se@SiO<sub>2</sub> nanospheres exhibited a zeta potential of  $-39.6$  mV, and the Se@PSN showed a less negative potential of  $-13.5$  mV (Figure S2). The coating of PVP on the silanol groups of the PSN surface reduced the toxicity of Se@PSN, and the increase in zeta potential facilitated improved cellular uptake of the nanoparticles. XRD patterns confirmed the crystalline structure of Se@PSN, showing characteristic peaks corresponding to the standard Se phase (JCPDS card No. 65–1876) and increased intensity in the low-angle region, likely due to amorphous silica (Figure 1D). Elemental mapping showed the distribution of Si, O, and Se within Se@PSN (Figure 1E). AFM analysis demonstrated a rough surface morphology of Se@PSN, with Rq and Ra values measuring 23.954 nm and 19.357 nm, respectively (Figure 1F and G). The nitrogen adsorption isotherm confirmed the mesoporous nature of Se@PSN, revealing a specific surface area of  $126.15$  m<sup>2</sup> g<sup>-1</sup> (Figure 1H, Figure S3). Barrett-Joyner-Halenda (BJH) analysis provided further details on the pore size distribution, with cumulative pore volume of  $0.311$  cm<sup>3</sup> g<sup>-1</sup> (Figure 1I and J). These findings corroborate the successful synthesis of Se@PSN.

The selenium release profile from Se@PSN in PBS was investigated, showing an initial rapid release that gradually decelerated over the subsequent days. After a period of five days, the selenium concentration released from an  $8$  g L<sup>-1</sup> Se@PSN suspension reached  $21.7$  mg L<sup>-1</sup> (Figure 1K). Dynamic light scattering (DLS) analysis showed an increase in average diameter from 63 nm for solid Se@SiO<sub>2</sub> to 85 nm for Se@PSN (Figure S4). The consistency of their mean diameter over the 14-day observation period further confirms the stability of Se@PSN (Figure 1L). Therefore, we applied them for cell or animal treatment within 14 days after synthesis.

The antioxidant capacity of Se@PSN was assessed through a series of assays (Figure 1M). Free radical inhibition tests demonstrated a dose-dependent enhancement of antioxidant activity, with Se@PSN showing stronger antioxidant properties compared to unetched Se@SiO<sub>2</sub>. ROS detection assays confirmed that Se@PSN effectively suppressed multiple types of ROS, including hydroxyl radicals ( $\bullet$ OH), superoxide anions ( $\bullet$ O<sub>2</sub><sup>-</sup>), and hydrogen peroxide (H<sub>2</sub>O<sub>2</sub>), with a dose-dependent effect for each ROS type.

## Pharmacokinetics and Biocompatibility of Se@PSN

To trace Se@PSN in cells and tissues, we aminated Se@PSN using APTES and conjugated it with FITC. To evaluate Se@PSN retention in reperfused myocardium, FITC-Se@PSN was immediately injected into the left ventricular wall of mice following the LAD coronary artery ligation. Fluorescence intensity in the injection site was measured at various time points using ex vivo fluorescence imaging. We found that FITC-Se@PSN remained at the injection site for up to 12 hours, with fluorescence intensity gradually decreasing by 24 hours and disappearing completely by 48 hours (Figure 2A). Selenium levels in the myocardium were also measured at these intervals using ICP-MS, revealing significantly elevated selenium concentrations at 12 hours post-injection, which decreased at 24 hours and returned to baseline by 48 hours (Figure 2D). These results indicate that Se@PSN can persist in myocardial tissue for up to 24 hours and is fully cleared within 48 hours.

To evaluate potential toxicity, Se@PSN was injected into the hearts of healthy mice, and various parameters were monitored over a 14-day period, as subsequent in vivo experiments did not exceed this duration. Histological analysis of the heart, liver, spleen, lungs, and kidneys at 1, 7, and 14 days post-injection showed no significant tissue damage in the Se@PSN-treated mice, compared to the control group (Figure 2B). Serum biochemical markers for liver function, including ALT and AST, as well as kidney function markers, such as BUN and CREA, indicated no adverse effects to liver and kidney from Se@PSN (Figure 2C). Additionally, to assess the impact of a higher dose of Se@PSN, an 8-fold higher dose than the therapeutic dose was injected into the myocardium. No elevation in myocardial injury markers such as serum LDH, CK-MB, and cTnI was observed, and no decline in myocardial contractile function was noted either 1 or 14 days post-injection (Figure S5). These results confirm that Se@PSN does not cause significant short-term or long-term toxicity to the heart or other major organs following myocardial injection.

In vitro cytotoxicity of Se@PSN was evaluated by exposing H9c2 cells to various concentrations of Se@PSN for 24 hours. Cell viability assays showed low cytotoxicity for Se@PSN, with significant impact only at  $160$  μg mL<sup>-1</sup> (Figure 2E). Moreover, among the various concentrations of Se@PSN tested,  $80$  μg/mL showed the strongest therapeutic effect on HR-treated H9c2 cells (Figure 2F). Consequently, we selected  $80$  μg mL<sup>-1</sup> as the treatment concentration for cell experiments. At this concentration, fluorescence microscopy confirmed progressive cellular uptake of FITC-Se@PSN after 3 hours of treatment, and it was retained within the cells for an extended period, indicating efficient cellular uptake by cardiomyocytes (Figure 2G).

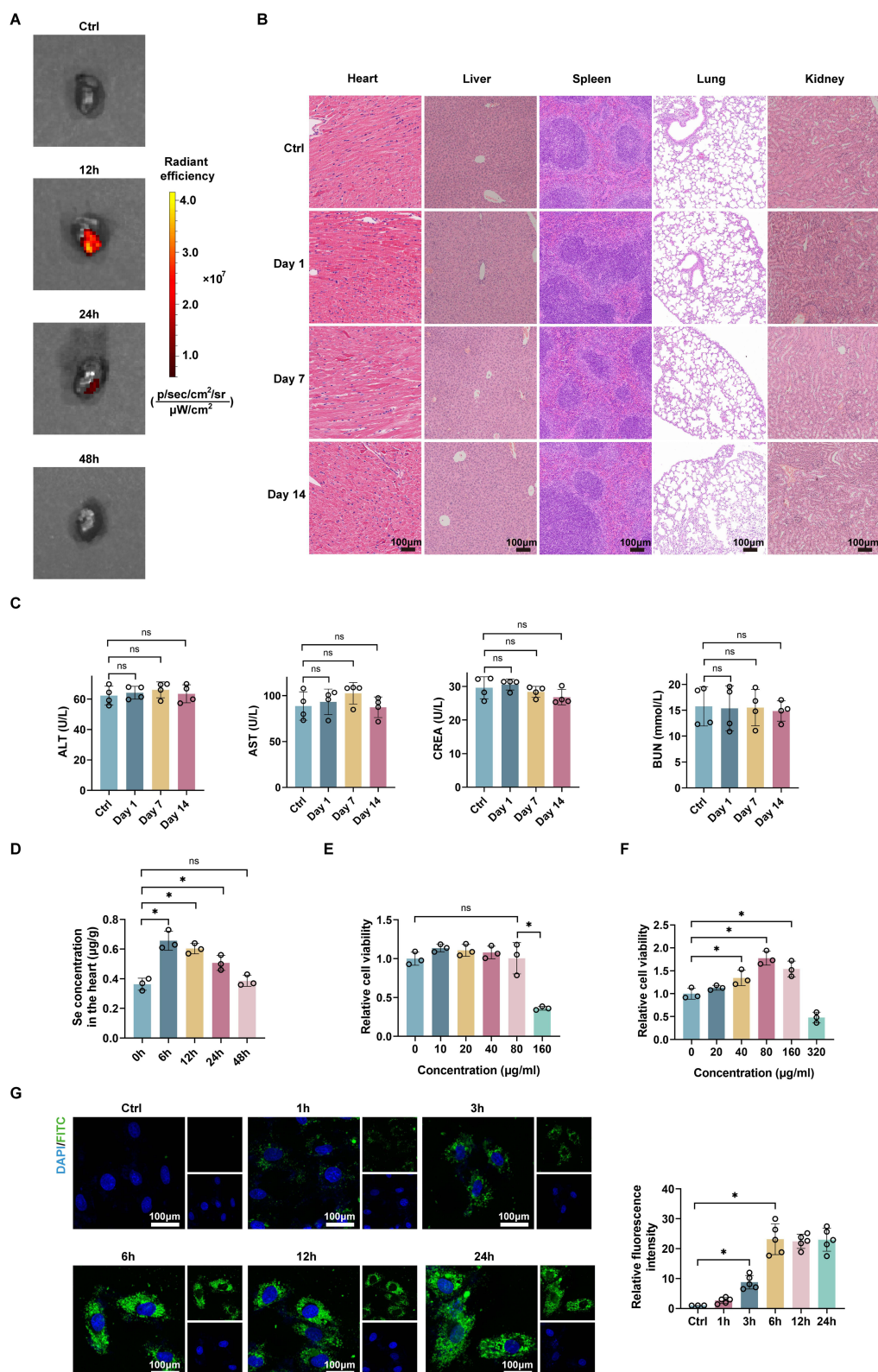


**Figure 2** Pharmacokinetics and Biocompatibility of Se@PSN. **(A)** Ex vivo fluorescence imaging of heart treated with IR following Se@PSN administration at different time. **(B)** H&E staining of heart, liver, spleen, lung, and kidney tissues from control and Se@PSN-treated groups at different time. **(C)** Serum levels of ALT, AST, CREA, and BUN in control and Se@PSN-treated mice at different time (n=4; ns, p>0.05). **(D)** Time-dependent selenium concentration in the heart from mice treated with IR following Se@PSN administration (n=3, \*p < 0.05). **(E)** Relative cell viability of cells treated with Se@PSN, as measured by CCK8 assay (n=3, \*p < 0.05). **(F)** Relative cell viability of HR-treated H9c2 cells after treatment with different concentrations of Se@PSN (n=3, \*p < 0.05). **(G)** Fluorescence imaging of FITC-Se@PSN in H9c2 cells at different time points post-treatment (n=3-5, \*p < 0.05).



between the two groups, indicating significant transcriptional changes induced by Se@PSN treatment (Figure 3B). Pearson correlation analysis confirmed high reproducibility and consistency among biological replicates (Figure S6). Differential expression gene (DEG) analysis identified 323 upregulated and 368 downregulated genes in the IR+Se@PSN group compared to the IR group (Figure 3C, Figure S7).

As expected, Se@PSN treatment led to altered expression of key ferroptosis-related genes, such as Gpx4, Ppara, and Ftl1, with their levels significantly increased in the Se@PSN-treated group, while Cybb and Trp53 levels were reduced (Figure 3D). Additionally, genes associated with the mitochondrial inner membrane and OXPHOS, including Hmgcs2, Cpt2, and several mtDNA-encoded genes, were also affected by Se@PSN treatment, suggesting that Se@PSN may help preserve mitochondrial structure and function (Figure 3E). This finding is supported by Gene Set Enrichment Analysis (GSEA), which showed significant enrichment of OXPHOS pathways in the IR+Se@PSN group (Figure 3F). Gene Ontology (GO) analysis of the DEGs highlighted enrichment in biological processes (BP) related to cellular respiration and respiratory ETC, as well as cellular components (CC) associated with the organelle inner membrane and mitochondrial inner membrane (Figure 3G). These results suggest that Se@PSN treatment after IR may mitigate ferroptosis and protect mitochondrial function.

In addition to its effects on ferroptosis and OXPHOS pathways, Se@PSN also regulated genes involved in oxidoreductase activity and oxidative stress (Figure 3D). GSEA further confirmed the regulatory effects of Se@PSN on these pathways (Figure S8). KEGG pathway analysis of DEG enrichment showed that genes involved in cardiac muscle contraction and calcium signaling, both of which are closely linked to heart function, were also influenced by Se@PSN treatment (Figure 3H). Protein-protein interaction (PPI) network analysis revealed that ferroptosis was closely interconnected with other key gene sets related to myocardial IR injury, indicating that ferroptosis may play a crucial role in Se@PSN's therapeutic effects (Figure 3I). Overall, these results provide valuable insights into the molecular mechanisms of Se@PSN-mediated cardioprotection, highlighting its potential to modulate critical pathways related to ferroptosis, mitochondrial OXPHOS, and oxidative stress response.

## Effects of Se@PSN on Ferroptosis in IR Injury

The RNA-seq results support our hypothesis that Se@PSN can reduce IR-induced ferroptosis. To further investigate, we examined myocardium ferroptosis levels following IR and Se@PSN treatment. The SLC7A11/GPX4 axis is the primary anti-ferroptotic pathway. In the IR group, GPX4 and SLC7A11 levels were significantly reduced, while Se@PSN treatment restored their expression, indicating that Se@PSN mitigates ferroptosis (Figure 4A and C). This was further confirmed by immunohistochemistry staining, which revealed increased GPX4 expression in the heart tissues of the IR+Se@PSN group compared to the IR and IR+PSN groups (Figure 4B). Additionally, glutathione peroxidase (GPx) activity in myocardium was also measured, showing that Se@PSN significantly enhanced GPx activity (Figure 4D). Given that lipid peroxidation is a hallmark of ferroptosis, we assessed the expression of the Ptg2, which encodes the key enzyme COX2 involved in the lipid peroxidation process. Ptg2 mRNA levels were significantly elevated in the IR group compared to controls, but notably decreased in the IR+Se@PSN group, suggesting a reduction in lipid peroxidation (Figure 4E).

We also confirmed Se@PSN's anti-ferroptotic effects *in vitro*. Ferroptosis was induced in H9c2 cells using erastin, with or without Se@PSN treatment. Consistent with *in vivo* experiments, erastin reduced the levels of GPX4 and SLC7A11 of H9c2 cells, while Se@PSN partially restored their expression (Figure S9). Accumulation of intracellular ferrous ions is a key feature of ferroptosis. Using FerroOrange, a fluorescent probe that generates orange fluorescence in the presence of free ferrous ions, we observed that Se@PSN significantly reduced ferrous ion accumulation in H9c2 cells, indicating a decrease in erastin-induced ferroptosis (Figure 4F and H). Lipid peroxidation was assessed in H9c2 cells using BODIPY-C11, a fluorescent probe that shifts from red to green upon oxidation during lipid peroxidation. Cells treated with erastin+Se@PSN showed reduced lipid peroxidation, as indicated by lower green fluorescence compared to the erastin and erastin+PSN groups (Figure 4G and I). This was further supported by Se@PSN's ability to reduce erastin-induced Ptg2 mRNA expression (Figure S10).

The PI3K/Akt pathway is a critical intracellular signaling cascade involved in regulating various cellular processes, and its activation has been shown to inhibit ferroptosis.<sup>26</sup> GSEA demonstrated that Se@PSN treatment activated the Akt signaling pathway (Figure 4I, Figure S11). Akt phosphorylates GSK3 $\beta$ , a kinase that inhibits the SLC7A11/GPX4 axis,

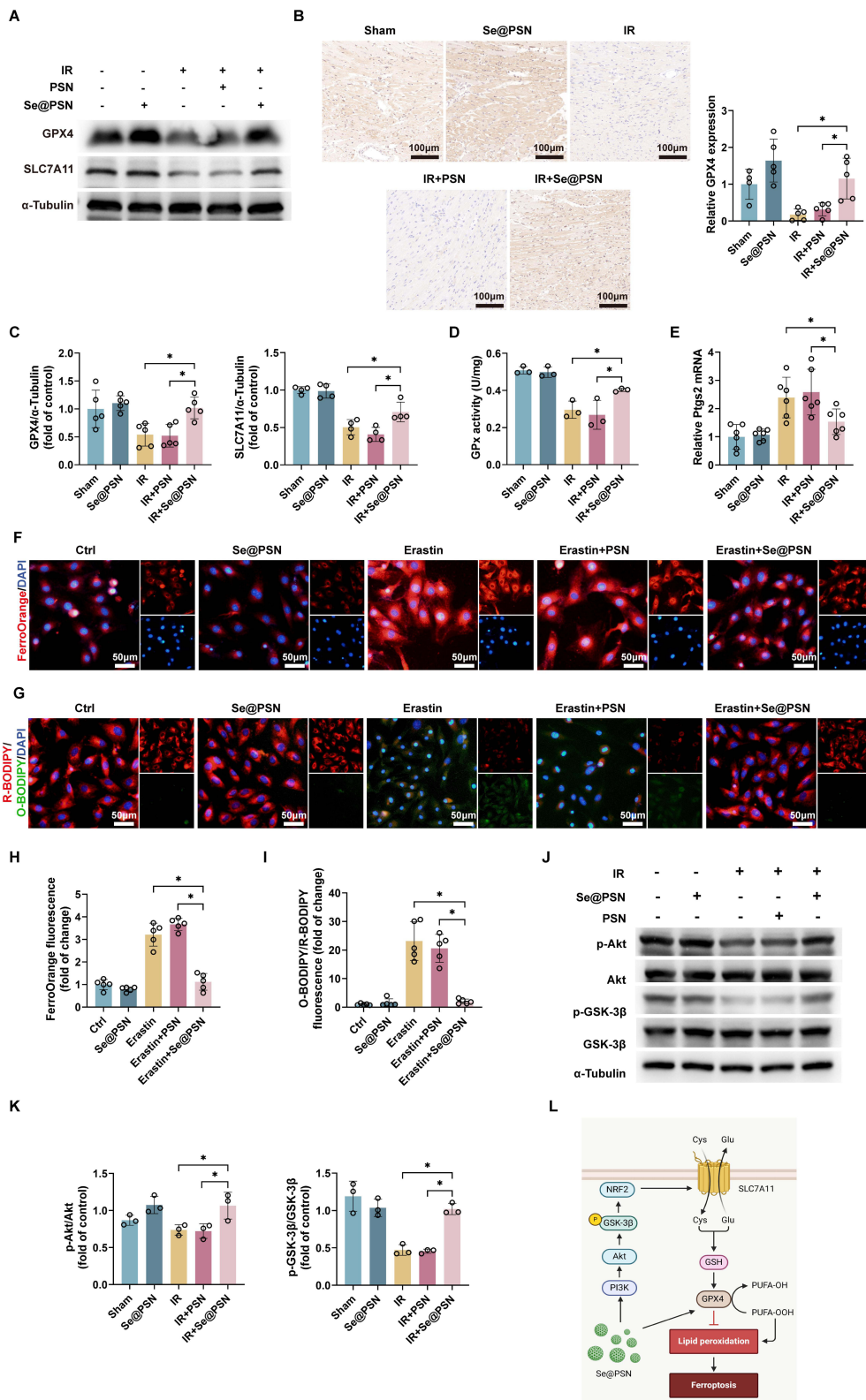


**Figure 4** Effects of Se@PSN on Ferroptosis in IR Injury. **A**, **(C)** Western blot images and quantification showing the expression levels of GPX4 and SLC7A11 in sham, Se@PSN, IR, IR+PSN, and IR+Se@PSN groups (n=4-5, \*p < 0.05). **(B)** Immunohistochemistry staining images and quantification of GPX4 in myocardium from different groups (n=4-5, \*p < 0.05). **(D)** Measurement of GPx activities in myocardium from different groups (n=3, \*p < 0.05). **(E)** Relative Prgs2 mRNA levels in myocardium from different groups (n=6, \*p < 0.05). **(F and H)** FerroOrange staining showing ferrous ions levels in H9c2 cells from control, Se@PSN, erastin, erastin+PSN, and erastin+Se@PSN groups (n=5, \*p < 0.05). **(G and I)** BODIPY-C11 staining demonstrating lipid peroxidation levels in H9c2 cells from different groups (n=5, \*p < 0.05). **J**, **(K)** Western blot analysis of phosphorylated and total Akt and GSK-3 $\beta$  in myocardium from different groups (n=3, \*p < 0.05). **(L)** Mechanism by which Se@PSN alleviates ferroptosis. Created in BioRender. Li, T. (2025) <https://BioRender.com/y58m263>.

resulting in its subsequent degradation. Therefore, we assessed the effect of Se@PSN on the activation of the PI3K/Akt/GSK3 $\beta$  pathway. Results showed that Se@PSN increased the phosphorylation of Akt and GSK-3 $\beta$  in the myocardium of the IR+Se@PSN group compared to the IR and IR+PSN groups (Figure 4J and K). Similar results were observed in H9c2 cells treated with erastin and Se@PSN (Figure S12). In summary, Se@PSN has the potential to reduce ferroptosis in cardiomyocytes induced by IR (Figure 4I).

## Impact of Se@PSN on Mitochondria in IR Injury

Mitochondrial dysfunction is closely associated with ferroptosis. Building on the RNA-seq results, we analyzed various parameters to investigate the impact of Se@PSN on mitochondrial function. In the IR group, the mRNA levels of key OXPHOS-related genes (mt-Co1, mt-Nd1, mt-Cytb, and mt-Atp6) were significantly downregulated compared to the sham group. However, Se@PSN treatment partially restored the expression of these genes, in contrast to PSN (Figure 5A). Similarly, Western blot analysis showed decreased levels of representative proteins from complexes I–V of the OXPHOS system in the IR group, while Se@PSN treatment restored these protein levels, underscoring Se@PSN's protective effect on mitochondrial complexes (Figure 5B and C). Furthermore, PGC-1 $\alpha$  levels were increased in the myocardium of the IR+Se@PSN group compared to the IR and IR+PSN groups (Figure S13). PGC-1 $\alpha$ , a co-transcriptional regulator of mitochondrial biogenesis, induces the transcription of multiple OXPHOS-related genes. During ferroptosis, PGC-1 $\alpha$  is degraded, exacerbating OXPHOS damage in myocardial IR injury.<sup>27</sup> It is proposed that the protection of mitochondrial respiratory complexes by Se@PSN is partially mediated through its inhibition of ferroptosis, which subsequently increases PGC-1 $\alpha$  levels.

Meanwhile, mitochondrial dynamics are also closely linked to ferroptosis, with excessive mitochondrial fission often observed during this process. An imbalance between mitochondrial fission and fusion leads to OXPHOS dysfunction and abnormal mitochondrial morphology, contributing to mitochondrial damage. Key proteins involved in mitochondrial fusion include MFN1 and OPA1, while DRP1 and FIS1 mediate mitochondrial fission. Our analysis revealed that IR treatment disrupted the balance between mitochondrial fusion and fission, as indicated by decreased MFN1 and OPA1 levels and increased FIS1 and p-DRP1 levels. Se@PSN treatment partially reversed these changes, promoting mitochondrial fusion and inhibiting excessive fission (Figure 5D and F). TEM images revealed that IR caused significant disruption to mitochondrial cristae structure and integrity, which were notably alleviated by Se@PSN treatment. Furthermore, IR resulted in myocardial myofibril rupture and dissolution, along with interstitial myocardial edema. In contrast, the IR+Se@PSN group exhibited tighter myofibrils, with reduced myofibril rupture and dissolution, indicating that Se@PSN has a protective effect on the myocardium (Figure 5E).

Partial restoration of OXPHOS and mitochondrial dynamics can reduce mitochondrial ROS production during IR. MitoSOX staining showed that Se@PSN significantly reduced mitochondrial ROS levels induced by HR treatment (Figure 5G and J). Excessive mitochondrial ROS can trigger the opening of the mPTP, resulting in proton influx and the collapse of the mitochondrial membrane potential. This sequence of events further damages mitochondrial respiratory function. In H9c2 cells, HR treatment resulted in a significant increase in mPTP opening, while Se@PSN treatment markedly reduced this opening (Figure 5H and K). The mitochondrial membrane potential of H9c2 cells was assessed using JC-1 staining. HR treatment led to a significant loss of membrane potential, whereas Se@PSN treatment effectively restored it (Figure 5I and L). These findings demonstrate that Se@PSN effectively preserves mitochondrial OXPHOS and dynamics, while reducing mitochondrial dysfunction (Figure 5M).

## Antioxidant Activity of Se@PSN in Cardiomyocytes

Both ferroptosis and OXPHOS damage compromise cell integrity by inducing oxidative stress; therefore, enhancing antioxidant capacity is crucial for protecting cardiomyocytes. Given Se@PSN's impact on ferroptosis and mitochondria, as well as its intrinsic reductive properties, we further explored whether Se@PSN could enhance the antioxidant capacity of cardiomyocytes. DCFH-DA staining images revealed elevated ROS levels in HR-treated cells, which were significantly reduced by Se@PSN treatment (Figure 6A and C). Additionally, HR treatment induced a significant decrease in the expression of the antioxidant protein NRF2; however, this reduction was partially reversed by Se@PSN, indicating its antioxidant effect (Figure 6B and D). The *in vivo* effects of Se@PSN on antioxidant protein expression and activity were

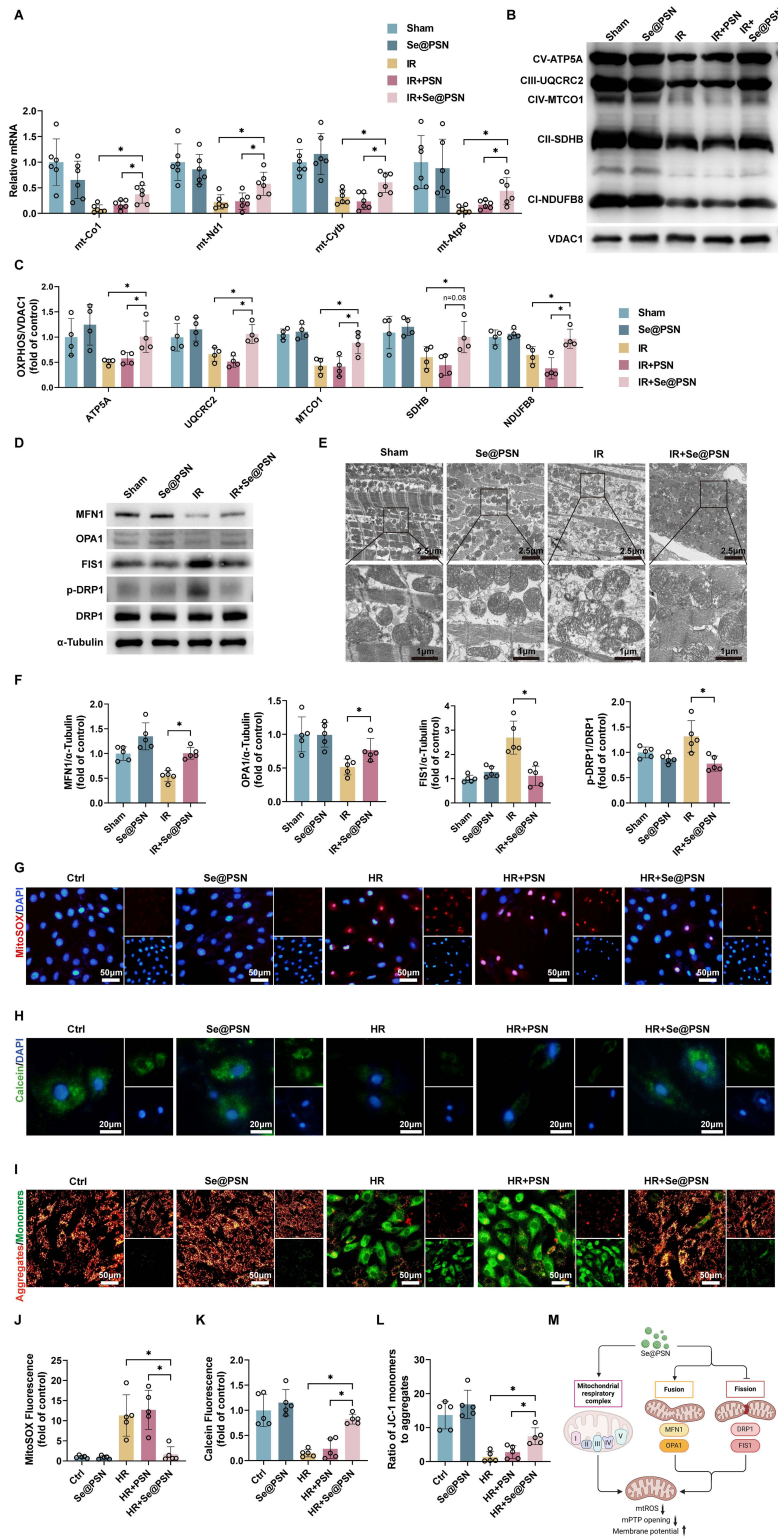


**Figure 5** Impact of Se@PSN on Mitochondria in IR Injury. **(A)** Relative mRNA levels of mt-CoI, mt-NdI, mt-Cytb, and mt-Atp6 in myocardium from sham, Se@PSN, IR, IR+PSN, and IR+Se@PSN groups (n=6, \*p < 0.05). **B, (C)** Western blot images and quantification of representative OXPHOS components (ATP5A, UQCRC2, MTCO1, SDHB, NDUFB8) in myocardium from different groups (n=4, \*p < 0.05). **(D, F)** Western blot images and quantification of mitochondrial dynamics proteins (MFN1, OPA1, FIS1, p-DRP1) in myocardium from different groups (n=5, \*p < 0.05). **(E)** TEM images of mitochondrial structures and myocardial fiber structure in myocardium from different groups. **(G and J)** MitoSOX staining images and quantitative analysis, demonstrating mitochondrial ROS level changes in H9c2 cells from control, Se@PSN, HR, HR+PSN, and HR+Se@PSN groups (n=5, \*p < 0.05). **(H and K)** Calcein AM staining for mPTP opening in H9c2 cells from different groups, with quantitative analysis of fluorescence intensity (n=5, \*p < 0.05). **(I and L)** JC-1 staining images and quantitative analysis, showing mitochondrial membrane potential changes in H9c2 cells from different groups (n=5, \*p < 0.05). **(M)** Mechanism by which Se@PSN protects mitochondria. Created in BioRender. Li, T. (2025) <https://BioRender.com/a41f268>.

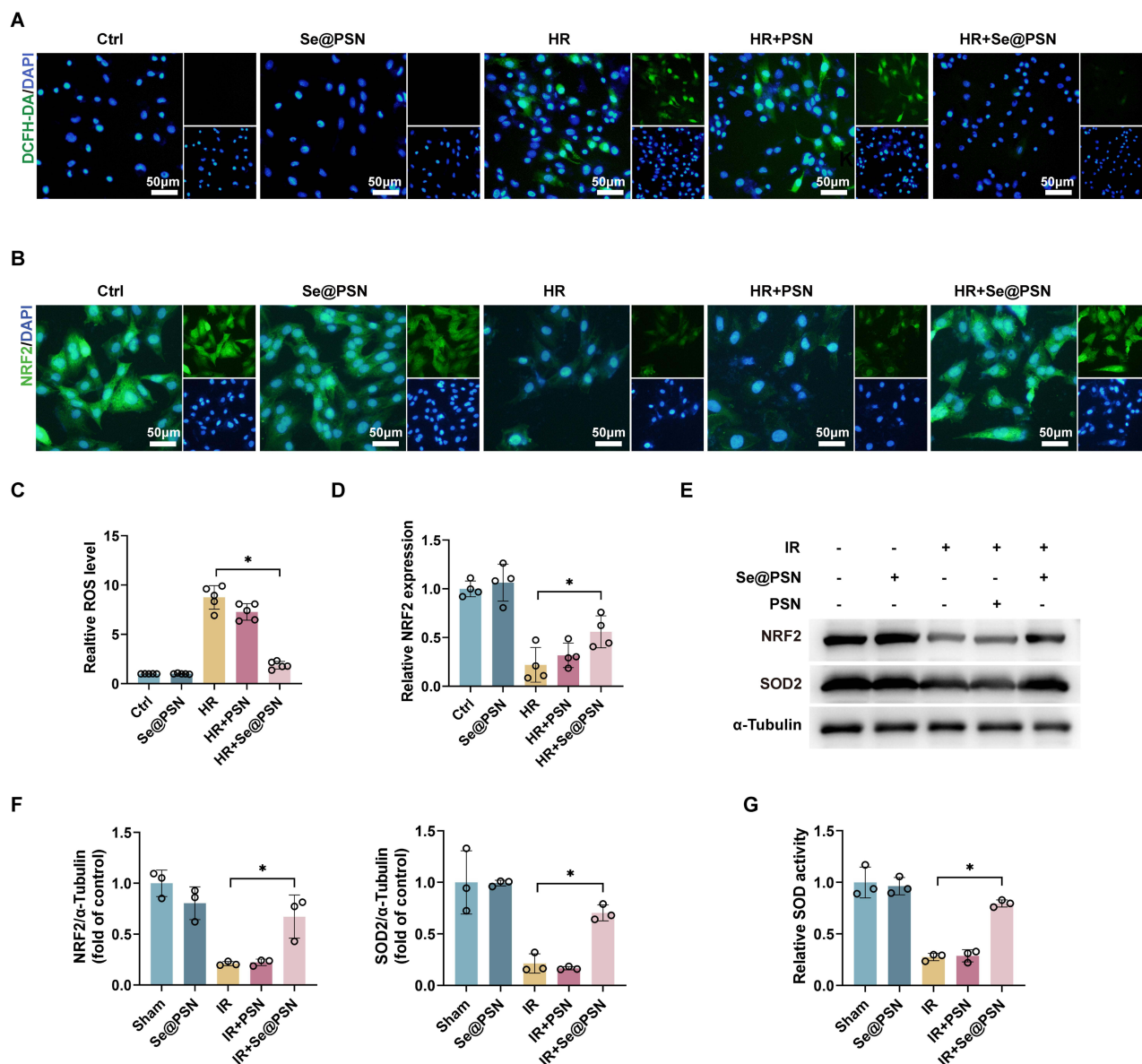


**Figure 6** Antioxidant Activity of Se@PSN in Cardiomyocytes. (**A** and **C**) ROS levels in H9c2 cells of the control, Se@PSN, HR, HR+PSN, and HR+Se@PSN groups ( $n=5$ ,  $*p < 0.05$ ). (**B** and **D**) NRF2 expression in H9c2 cells of different groups ( $n=4-6$ ,  $*p < 0.05$ ). (**E** and **F**) Western blot analysis of NRF2 and SOD2 expression in the myocardium from Sham, Se@PSN, IR, IR+PSN, and IR+Se@PSN groups ( $n=3$ ,  $*p < 0.05$ ). (**G**) Measurement of SOD activity in the myocardium from different groups ( $n=3$ ,  $*p < 0.05$ ).

also evaluated in mice subjected to myocardial IR treatment. The IR+Se@PSN group showed higher expressions of NRF2 and SOD2 compared to the IR and IR+PSN groups (Figure 6E and F). Additionally, Se@PSN alleviated the IR-induced reduction in SOD activity (Figure 6G). These analyses demonstrated that Se@PSN effectively reduced oxidative stress and promoting cellular antioxidant defenses of cardiomyocytes.

## Cardioprotective Effects of Se@PSN in IR Injury

On the first day after IR, we measured several indicators to evaluate myocardial injury. Echocardiographic analysis showed that the IR+Se@PSN group exhibited significantly improved cardiac function compared to the IR and IR+PSN groups, with higher ejection fraction (EF) and fractional shortening (FS) (Figure 7A and B). Infarct size was also markedly reduced in the IR+Se@PSN group, with similar areas at risk in both groups, as determined by TTC & Evans

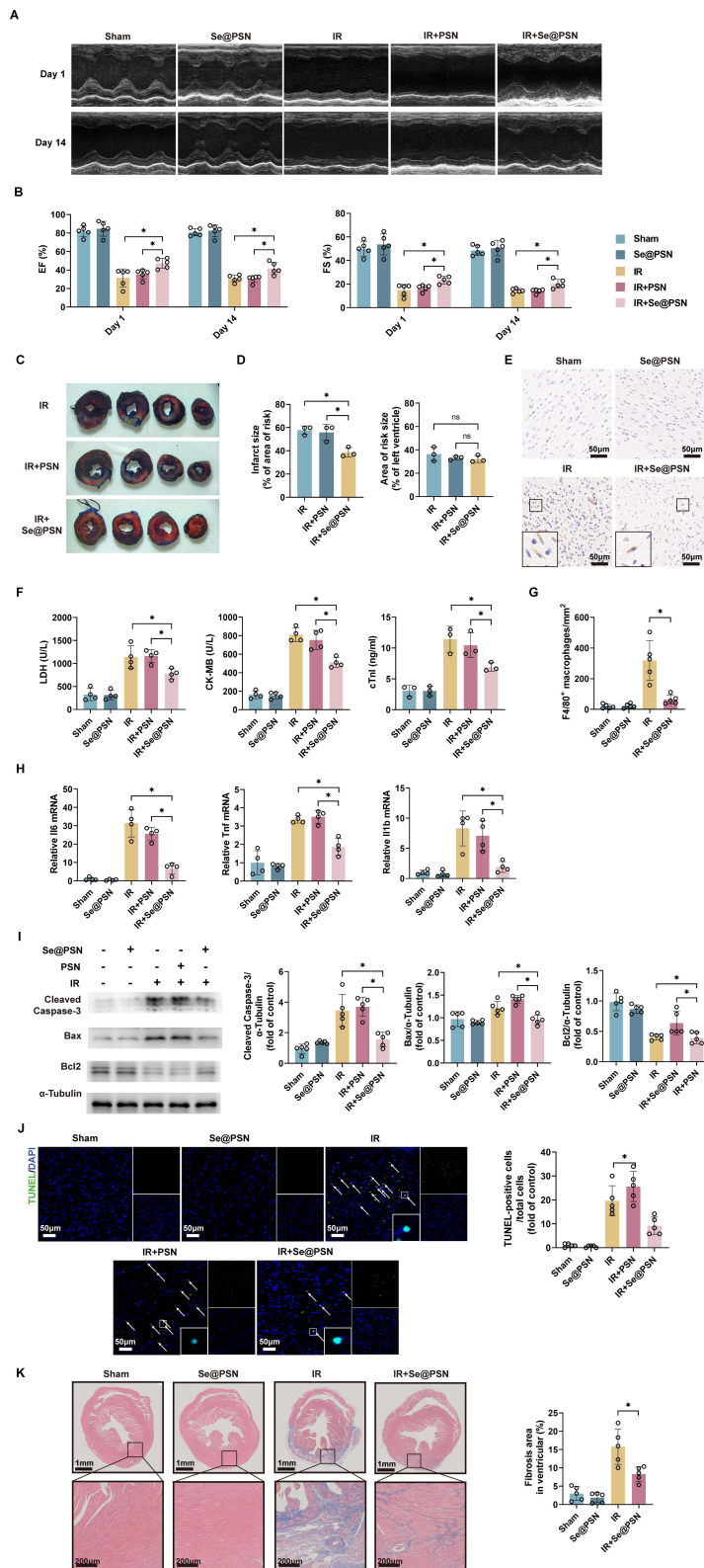


**Figure 7** Cardioprotective Effects of Se@PSN in IR Injury. **(A)** Echocardiography images of mice from Sham, Se@PSN, IR, IR+PSN, and IR+Se@PSN groups at day 1 and 14 post-IR. **(B)** EF and FS of hearts at day 1 and 14 post-IR from different groups (n=5, \*p < 0.05). **(C)** TTC & Evans Blue stained heart sections from IR, IR+PSN, and IR+Se@PSN groups. **(D)** Measurement of infarct and risk area sizes of myocardium from different groups (n=3, \*p < 0.05). **(E and G)** Immunohistochemical staining images and quantification for F4/80 positive cells in myocardium from different groups (n=5, \*p < 0.05). **(F)** Serum levels of cardiac injury markers in mice from different groups (n=3-4, \*p < 0.05). **(H)** Relative mRNA levels of inflammatory cytokine including Il6, Tnf, and Il1b in myocardium from different groups (n=4, \*p < 0.05). **(I)** Western blot images and quantification of cleaved Caspase-3, Bax, and Bcl2 in myocardial from different groups (n=5, \*p < 0.05). **(J)** TUNEL staining image and quantification of myocardial from different groups (n=5, \*p < 0.05). **(K)** Masson's trichrome staining of myocardial from different groups and fibrosis area quantification in the left ventricle (n=5, \*p < 0.05).

Blue staining (Figure 7C and D). Serum levels of several cardiac injury markers including LDH, CK-MB, and cTnI were lower in the IR+Se@PSN group, indicating less myocardial damage (Figure 7F). Myocardial damage caused by IR injury triggers an inflammatory response, which plays a critical role in the extent of damage and prognosis. Histological analysis shows that macrophage infiltration, an important marker for inflammation, was reduced in the IR+Se@PSN group on day 1 post-IR (Figure 7E and G). Additionally, Se@PSN treatment reduced the transcription of pro-inflammatory genes *Il6*, *Tnfa*, and *Il1b* in the myocardium, suggesting an anti-inflammatory effect (Figure 7H). Apoptosis levels were also evaluated, showing reduced expression of the pro-apoptotic proteins Bax and cleaved Caspase-3, alongside increased levels of the anti-apoptotic protein Bcl2 in the IR+Se@PSN group (Figure 7I). TUNEL staining confirmed fewer apoptotic cells in the IR regions following Se@PSN treatment, further supporting the anti-apoptotic effect (Figure 7J). These findings were corroborated by *in vitro* experiments (Figure S14). Collectively, these data demonstrate that Se@PSN treatment during IR reduces myocardial cell loss, alleviates inflammation, and preserves cardiac function in the early stages of IR injury.

Following IR injury, cardiac fibroblasts are activated, leading to excessive fibrosis at the reperfusion site. Around two weeks post-IR, pathological remodeling occurs in the damaged area, with the extent of fibrosis influenced by the severity of the initial injury and the inflammatory response. Echocardiographic analysis on day 14 post-IR showed that the IR+Se@PSN group had significantly higher EF and FS compared to the IR group (Figure 7A and B). Furthermore, the left ventricular volumes in diastole (LV Vol;d) and systole (LV Vol;s) were significantly lower in the IR+Se@PSN group, suggesting reduced cardiac failure in the later stages of injury (Figure S15). Masson's trichrome staining revealed decreased fibrosis in the IR+Se@PSN group, with lower expression of fibrosis markers *Col1a1* and *Col3a1* compared to the IR group, indicating that Se@PSN treatment attenuated late-stage cardiac pathological remodeling (Figure 7K, Figure S16).

## Discussion

Cardiovascular diseases are the leading cause of death and disability worldwide, and myocardial IR injury is an unavoidable complication during treatment. Inhibiting ferroptosis has emerged as a novel strategy to reduce cardiomyocyte death and improve outcomes in IR injury. In this study, we synthesized Se@PSN to treat IR injury. Se@PSN demonstrated excellent absorption efficiency and biocompatibility both *in vitro* and *in vivo*. Due to its reductive properties, Se@PSN effectively scavenged various ROS, enhancing the antioxidant capacity of cardiomyocytes. More importantly, Se@PSN significantly reduced ferroptosis and mitochondrial damage during IR. These findings suggest that Se@PSN holds great potential for mitigating myocardial injury induced by IR through ferroptosis inhibition and mitochondrial function preservation.

Ferroptosis, a form of regulated cell death discovered in recent years, is driven by the accumulation of lipid peroxides due to GPX4 inactivation and iron overload. Recent studies have identified ferroptosis as a key contributor to cardiac diseases, particularly IR injury.<sup>28,29</sup> During myocardial IR injury, ferritinophagy is upregulated, leading to dysregulation of iron transport proteins such as ferroportin (FPN) and transferrin receptor 1 (TFR1).<sup>30,31</sup> This results in excess iron accumulation in cardiomyocytes under IR conditions, which then produces ROS through the Fenton reaction. During ferroptosis, ROS induce the peroxidation of polyunsaturated fatty acids, especially arachidonic acids (AAs), leading to damage of the lipid bilayer. The SLC7A11/ GPX4 axis is the primary pathway for inhibiting ferroptosis.<sup>32</sup> Under normal physiological conditions, GPX4 uses GSH to reduce phospholipid hydroperoxides (PLOOHs) to non-toxic phospholipid alcohols (PLOHs), preventing lipid peroxidation.<sup>33</sup> In myocardial IR injury, the reduction of SLC7A11 and GPX4 impairs this pathway, triggering ferroptosis. Mice overexpressing GPX4 exhibit reduced cardiomyocyte ferroptosis during IR injury.<sup>34</sup> Selenium is crucial for the redox activity of GPX4, and mutation of selenocysteine to cysteine reduces GPX4 catalytic activity by 90%. Adequate selenium supplementation can also enhance the stability and translation efficiency of Gpx4 mRNA.<sup>35</sup> Our data show that Se@PSN effectively leads to increased levels of GPX4, GSH, and selenium in the heart. Se@PSN releases selenium quantum dots within cardiomyocytes, and the elevated selenium concentration may enhance GPX4 expression by improving the translation efficiency of Gpx4 mRNA and increasing the synthesis of selenium-modified cysteine. This treatment also reduces iron ion accumulation, ROS production, and lipid peroxidation in cardiomyocytes following IR injury. These findings indicate that Se@PSN can inhibit ferroptosis in cardiomyocytes caused by IR. Notably, although SLC7A11 is not a selenoprotein, Se@PSN was still

able to increase SLC7A11 protein levels in cardiomyocytes. This effect is likely mediated through the activation of the PI3K/Akt/GSK-3 $\beta$  pathway. Studies have shown that GSK-3 $\beta$  can phosphorylate NRF2, leading to its recognition by  $\beta$ -TrCP, which triggers its ubiquitination and proteasomal degradation.<sup>36</sup> The reduction of NRF2, in turn, leads to decreased transcription of SLC7a11. Our findings indicate that Se@PSN enhances the phosphorylation of Akt and GSK-3 $\beta$  in cardiomyocytes and increases intracellular NRF2 protein levels, which likely contributes to the upregulation of SLC7A11 expression.

Se@PSN has also been shown to reduce mitochondrial damage caused by IR injury. Mitochondria make up approximately 30% of the cardiomyocyte volume and are essential for maintaining cardiac energy metabolism and contractile function.<sup>37</sup> OXPHOS is a critical pathway for energy production in mitochondria, and mitochondrial respiratory defects during IR stress may result from significant reductions in OXPHOS integrity and mtDNA content.<sup>38</sup> When OXPHOS is compromised, electrons leak from the ETC and combine with oxygen, producing large amounts of ROS.<sup>39</sup> This excessive mitochondrial ROS generation triggers the opening of the mPTP.<sup>40–42</sup> mPTP is a high-conductance, non-specific channel in the mitochondrial inner membrane, and its opening causes a sudden increase in membrane permeability to solutes, resulting in the loss of mitochondrial membrane potential, swelling, and destruction.<sup>43</sup> Our findings suggest that Se@PSN preserves OXPHOS integrity in cardiomyocytes, while preventing IR-induced mitochondrial ROS production, mPTP opening, and membrane potential collapse.

Although Se@PSN was originally designed to mitigate ferroptosis, its ability to protect mitochondria during IR injury is not coincidental. Increasing evidence suggests a close connection between ferroptosis and mitochondrial damage. On one hand, ferroptosis acts as a driver of mitochondrial dysfunction. For example, the oxidation of arachidonic acid during ferroptosis produces 15-hydroperoxy-eicosatetraenoic acid (15-HpETE), which promotes the degradation of PGC-1 $\alpha$ , the transcription factor crucial for mitochondrial function. PGC-1 $\alpha$  activates NRF2, inducing the expression of proteins involved in the OXPHOS system.<sup>27</sup> The reduction of PGC-1 $\alpha$  during ferroptosis results in mitochondrial dysfunction, further impairing cardiac contractility. Our experiments confirmed that IR injury causes a decrease in PGC-1 $\alpha$  levels, whereas Se@PSN treatment preserves PGC-1 $\alpha$  expression. On the other hand, mitochondrial damage can also drive ferroptosis. Decreased SOD2 activity and OXPHOS disruption in damaged mitochondria lead to the accumulation of mitochondrial ROS, which triggers ferritinophagy.<sup>44</sup> Additionally, OXPHOS impairment disrupts the tricarboxylic acid (TCA) cycle, reducing intracellular NAD/NADP and cysteine levels. These molecules are critical for GSH synthesis and recycling, which are essential for controlling ferroptosis.<sup>45</sup> In summary, ferroptosis and mitochondrial damage are interdependent during myocardial IR injury, creating a vicious cycle.<sup>46,47</sup> While Se@PSN was designed to elevate GPX4 levels to reduce ferroptosis, given the complex interplay between mitochondrial damage and ferroptosis—as well as the diverse biological effects of selenium—it is unlikely that the mitochondrial protective effects are solely due to ferroptosis inhibition. Se@PSN may influence both OXPHOS and ferroptosis through multiple mechanisms, which warrants further investigation.

This study still has some limitations. First, although Se@PSN activates the PI3K/Akt/GSK-3 $\beta$  pathway, its underlying mechanism has not been explored. The mechanism by which Se@PSN protects the myocardium from IR injury may be more complex and requires further investigation. Second, the local myocardial delivery method used in this study was intramyocardial injection, which is not commonly applied in clinical practice. A better approach may involve intracoronary delivery using stents or balloons loaded with Se@PSN during coronary intervention procedures, as this would be more effective than systemic administration. We plan to conduct these studies in larger animal models. The aim of this study is to first establish the efficacy of Se@PSN for local treatment, laying the foundation for subsequent attempts at intracoronary administration.

## Conclusion

In conclusion, Se@PSN effectively alleviates ferroptosis, enhances mitochondrial function, and reduces ROS levels, showing great potential for clinical translation in ferroptosis-related diseases. In the mouse IR model, we demonstrated that Se@PSN significantly reduces cardiomyocyte death, myocardial fibrosis, and cardiac dysfunction, making it a promising therapeutic strategy for IR injury and offering new prospects for the development of nanomedicine.

## Acknowledgments

The picture in the graphical abstract, [Figures 4L](#) and [5M](#) was created with biorender.com (Taixi Li, with agreement numbers GH27VZ8MDX, PS27VZ8YDS, and JQ27VZ9CM3).

## Funding

This study is supported by grants from the National Natural Science Foundation of China (No. 8217051361).

## Disclosure

The authors report no conflicts of interest in this work.

## References

- Virani SS, Alonso A, Aparicio HJ, et al. Heart disease and stroke statistics-2021 update: a report from the American heart association. *Circulation*. 2021;143(8):e254–e743. doi:10.1161/CIR.0000000000000950
- Khan MA, Hashim MJ, Mustafa H, et al. Global epidemiology of ischemic heart disease: results from the global burden of disease study. *Cureus*. 2020;12(7):e9349. doi:10.7759/cureus.9349
- Tejedor S, Dolz-Pérez I, Decker CG, et al. Polymer conjugation of docosahexaenoic acid potentiates cardioprotective therapy in preclinical models of myocardial ischemia/reperfusion injury. *Adv. Healthcare Mater*. 2021;10(9):2002121. doi:10.1002/adhm.202002121
- Kajstura J, Cheng W, Reiss K, et al. Apoptotic and necrotic myocyte cell deaths are independent contributing variables of infarct size in rats. *Lab Invest*. 1996;74(1):86–107.
- Reed GW, Rossi JE, Cannon CP. Acute myocardial infarction. *Lancet*. 2017;389(10065):197–210. doi:10.1016/S0140-6736(16)30677-8
- Yellon DM, Hausenloy DJ. Myocardial reperfusion injury. *N Engl J Med*. 2007;357(11):1121–1135. doi:10.1056/NEJMra071667
- Zhou Y, Liang Q, Wu X, et al. siRNA delivery against myocardial ischemia reperfusion injury mediated by reversibly camouflaged biomimetic nanocomplexes. *Adv Mater*. 2023;35(23):e2210691. doi:10.1002/adma.202210691
- Konstantinidis K, Whelan RS, Kitsis RN. Mechanisms of cell death in heart disease. *Arterioscler Thromb Vasc Biol*. 2012;32(7):1552–1562. doi:10.1161/ATVBAHA.111.224915
- Whelan RS, Kaplinskiy V, Kitsis RN. Cell death in the pathogenesis of heart disease: mechanisms and significance. *Annu Rev Physiol*. 2010;72:19–44.
- Kang H, Meng F, Liu F, et al. Nanomedicines targeting ferroptosis to treat stress-related diseases. *Int J Nanomed*. 2024;19:8189–8210. doi:10.2147/IJN.S476948
- Lei W, Yang J, Wang J, et al. Synergetic EGCG and coenzyme Q10 DSPC liposome nanoparticles protect against myocardial infarction. *Biomater Sci*. 2023;11(20):6862–6870. doi:10.1039/D3BM00857F
- Fang X, Wang H, Han D, et al. Ferroptosis as a target for protection against cardiomyopathy. *Proc Natl Acad Sci U S A*. 2019;116(7):2672–2680. doi:10.1073/pnas.1821022116
- Liu Y, Wang S, Zhang J, et al. Reprogramming the myocardial infarction microenvironment with melanin-based composite nanomedicines in mice. *Nat Commun*. 2024;15(1):6651. doi:10.1038/s41467-024-50854-4
- Zhao T, Wu W, Sui L, et al. Reactive oxygen species-based nanomaterials for the treatment of myocardial ischemia reperfusion injuries. *Bioact Mater*. 2022;7:47–72. doi:10.1016/j.bioactmat.2021.06.006
- Zhang S, Zhang J, Fan X, et al. Ionizing radiation-induced ferroptosis based on nanomaterials. *Int J Nanomed*. 2022;17:3497–3507. doi:10.2147/IJN.S372947
- Chen X, Li W, Ren J, et al. Translocation of mixed lineage kinase domain-like protein to plasma membrane leads to necrotic cell death. *Cell Res*. 2014;24(1):105–121. doi:10.1038/cr.2013.171
- Ji X, Meng Y, Wang Q, et al. Cysteine-Based Redox-Responsive Nanoparticles for Fibroblast-Targeted Drug Delivery in the Treatment of Myocardial Infarction. *ACS Nano*. 2023;17(6):5421–5434. doi:10.1021/acsnano.2c10042
- Stolwijk JM, Falls-Hubert KC, Searby CC, Wagner BA, Buettner GR. Simultaneous detection of the enzyme activities of GPx1 and GPx4 guide optimization of selenium in cell biological experiments. *Redox Biol*. 2020;32:101518.
- Alim I, Caulfield JT, Chen Y, et al. Selenium drives a transcriptional adaptive program to block ferroptosis and treat stroke. *Cell*. 2019;177(5):1262–1279.e25. doi:10.1016/j.cell.2019.03.032
- Khurana A, Tekula S, Saifi MA, Venkatesh P, Godugu C. Therapeutic applications of selenium nanoparticles. *Biomed Pharmacother*. 2019;111:802–812.
- Huang Y, Lu G, Zhou L. A mini review on selenium quantum dots: synthesis and biomedical applications. *Front Bioeng Biotechnol*. 2023;11:1332993.
- Vivero-Escoto JL, Slowing II, Trewyn BG, Lin VS. Mesoporous silica nanoparticles for intracellular controlled drug delivery. *Small*. 2010;6(18):1952–1967. doi:10.1002/sml.200901789
- Popat A, Hartono SB, Stahr F, Liu J, Qiao SZ, Qing Max Lu G. Mesoporous silica nanoparticles for bioadsorption, enzyme immobilisation, and delivery carriers. *Nanoscale*. 2011;3(7):2801–2818. doi:10.1039/c1nr10224a
- Lu J, Liong M, Li Z, Zink JJ, Tamanoi F. Biocompatibility, biodistribution, and drug-delivery efficiency of mesoporous silica nanoparticles for cancer therapy in animals. *Small*. 2010;6(16):1794–1805. doi:10.1002/sml.201000538
- Liu X, Deng G, Wang Y, et al. A novel and facile synthesis of porous SiO<sub>2</sub>-coated ultrasmall Se particles as a drug delivery nanoplatfrom for efficient synergistic treatment of cancer cells. *Nanoscale*. 2016;8(16):8536–8541. doi:10.1039/C6NR02298G
- Jiang Y, Qiao Y, He D, Tian A, Li Z. Adaptor protein Hip-55-mediated signalosome protects against ferroptosis in myocardial infarction. *Cell Death Differ*. 2023;30(3):825–838. doi:10.1038/s41418-022-01110-z
- Cai W, Liu L, Shi X, et al. Alox15/15-HpETE aggravates myocardial ischemia-reperfusion injury by promoting cardiomyocyte ferroptosis. *Circulation*. 2023;147(19):1444–1460. doi:10.1161/CIRCULATIONAHA.122.060257

28. Sun Q, Ma H, Zhang J, et al. A self-sustaining antioxidant strategy for effective treatment of myocardial infarction. *Adv Sci (Weinh)*. 2023;10(5): e2204999. doi:10.1002/advs.202204999
29. Yin Z, Ding G, Chen X, et al. Beclin1 haploinsufficiency rescues low ambient temperature-induced cardiac remodeling and contractile dysfunction through inhibition of ferroptosis and mitochondrial injury. *Metabolism*. 2020;113:154397.
30. Li W, Li W, Wang Y, Leng Y, Xia Z. Inhibition of DNMT-1 alleviates ferroptosis through NCOA4 mediated ferritinophagy during diabetes myocardial ischemia/reperfusion injury. *Cell Death Discov*. 2021;7(1):267. doi:10.1038/s41420-021-00656-0
31. Fan Z, Cai L, Wang S, Wang J, Chen B. Baicalin prevents myocardial ischemia/reperfusion injury through inhibiting ACSL4 mediated ferroptosis. *Front Pharmacol*. 2021;12:628988.
32. Yang WS, SriRamaratnam R, Welsch ME, et al. Regulation of ferroptotic cancer cell death by GPX4. *Cell*. 2014;156(1):317–331. doi:10.1016/j.cell.2013.12.010
33. Frangogiannis NG. The inflammatory response in myocardial injury, repair, and remodeling. *Nat Rev Cardiol*. 2014;11(5):255–265. doi:10.1038/nrcardio.2014.28
34. Miyamoto HD, Ikeda M, Ide T, et al. Iron overload via heme degradation in the endoplasmic reticulum triggers ferroptosis in myocardial ischemia-reperfusion injury. *JACC Basic Transl Sci*. 2022;7(8):800–819. doi:10.1016/j.jacbts.2022.03.012
35. Xie Y, Kang R, Klionsky DJ, Tang D. GPX4 in cell death, autophagy, and disease. *Autophagy*. 2023;19(10):2621–2638. doi:10.1080/15548627.2023.2218764
36. Du Y, Zhou Y, Yan X, et al. APE1 inhibition enhances ferroptotic cell death and contributes to hepatocellular carcinoma therapy. *Cell Death Differ*. 2024;31(4):431–446. doi:10.1038/s41418-024-01270-0
37. Hall AR, Burke N, Dongworth RK, Hausenloy DJ. Mitochondrial fusion and fission proteins: novel therapeutic targets for combating cardiovascular disease. *Br J Pharmacol*. 2014;171(8):1890–1906. doi:10.1111/bph.12516
38. Zhang J, Liu L, Dong Z, et al. An ischemic area-targeting, peroxynitrite-responsive, biomimetic carbon monoxide nanogenerator for preventing myocardial ischemia-reperfusion injury. *Bioact Mater*. 2023;28:480–494.
39. Chen YR, Zweier JL. Cardiac mitochondria and reactive oxygen species generation. *Circ Res*. 2014;114(3):524–537. doi:10.1161/CIRCRESAHA.114.300559
40. Kühl I, Miranda M, Atanassov I, et al. Transcriptomic and proteomic landscape of mitochondrial dysfunction reveals secondary coenzyme Q deficiency in mammals. *Elife*. 2017;6: e30952.
41. Long X, Liu M, Nan Y, et al. Revitalizing ancient mitochondria with nano-strategies: mitochondria-remediating nanodrugs concentrate on disease control. *Adv Mater*. 2024;36(18):2308239. doi:10.1002/adma.202308239
42. Doll S, Freitas FP, Shah R, et al. FSP1 is a glutathione-independent ferroptosis suppressor. *Nature*. 2019;575(7784):693–698. doi:10.1038/s41586-019-1707-0
43. Morciano G, Bonora M, Campo G, et al. Mechanistic Role of mPTP in Ischemia-Reperfusion Injury. *Adv Exp Med Biol*. 2017;982:169–189.
44. Qin X, Zhang J, Wang B, et al. Ferritinophagy is involved in the zinc oxide nanoparticles-induced ferroptosis of vascular endothelial cells. *Autophagy*. 2021;17(12):4266–4285. doi:10.1080/15548627.2021.1911016
45. Ahola S, Langer T. Ferroptosis in mitochondrial cardiomyopathy. *Trends Cell Biol*. 2024;34(2):150–160. doi:10.1016/j.tcb.2023.06.002
46. Vásquez-Trincado C, García-Carvajal I, Pennanen C, et al. Mitochondrial dynamics, mitophagy and cardiovascular disease. *J Physiol*. 2016;594(3):509–525. doi:10.1113/JP271301
47. Peoples JN, Saraf A, Ghazal N, Pham TT, Kwong JQ. Mitochondrial dysfunction and oxidative stress in heart disease. *Exp Mol Med*. 2019;51(12):1–13. doi:10.1038/s12276-019-0355-7

International Journal of Nanomedicine

Publish your work in this journal

The International Journal of Nanomedicine is an international, peer-reviewed journal focusing on the application of nanotechnology in diagnostics, therapeutics, and drug delivery systems throughout the biomedical field. This journal is indexed on PubMed Central, MedLine, CAS, SciSearch®, Current Contents®/Clinical Medicine, Journal Citation Reports/Science Edition, EMBase, Scopus and the Elsevier Bibliographic databases. The manuscript management system is completely online and includes a very quick and fair peer-review system, which is all easy to use. Visit <http://www.dovepress.com/testimonials.php> to read real quotes from published authors.

Submit your manuscript here: <https://www.dovepress.com/international-journal-of-nanomedicine-journal>

**Dovepress**  
Taylor & Francis Group